Journal of Materials Chemistry A

ROYAL SOCIETY OF CHEMISTRY

PAPER

Cite this: *J. Mater. Chem. A*, 2024, **12**, 26013

Optimizing the thermoelectric performance of n-type PbSe through dynamic doping driven by entropy engineering†

Shujie Wu,[a] Changyuan Li,[c] Feida Chen,*[ab] Kun Yang,[ab] Chengchao Hu,[d] Haihua Huang,[d] Wenjing Huang,[a] Xueli Zuo[a] and Xiaobin Tang*[ab]

As an ideal candidate for PbTe, which maintains excellent performance at mid-temperature, PbSe holds great application potential. In this work, based on an optimized dynamic doping material system, a series of entropy-enhanced n-type lead chalcogenides $Pb_{1-y}Sn_ySe_{1-x}Te_xS_x$-2at%Cu ($x = 0$ and $y = 0$; $x = 0.1$ and $y = 0$; $x = 0.25$ and $y = 0$; $x = 0.25$ and $y = 0.125$) are synthesized. The thermoelectric properties of PbSe are modulated by gradually increasing its configurational entropy through alloying with Te/S/Sn. Research results show that the increase in configurational entropy improves the crystal symmetry of PbSe and significantly increases the Seebeck coefficient while maintaining good electrical properties. The dense dislocations and nanoscale to submicron-scale incoherent precipitates generated lead to the localization of phonons, increase anharmonicity, and reduce the lattice thermal conductivity at room temperature to 0.73 W m^{-1} K^{-1}. The total thermal conductivity drops significantly by 69.8%. Consequently, the thermoelectric properties of $Pb_{0.875}Sn_{0.125}Se_{0.5}Te_{0.25}S_{0.25}$–2at%Cu are remarkably improved, with a maximum dimensionless merit ZT_{max} of ~1.46 at 623 K and an average dimensionless merit ZT_{ave} of ~1.15 at 300–700 K. In addition, the room-temperature dimensionless merit ZT_{RT} ~0.64 is the highest reported for n-type PbSe. This optimization strategy of dynamic doping combined with entropy engineering to regulate electron and phonon transport demonstrates a feasible means to improve thermoelectric performance.

Received 21st June 2024
Accepted 20th August 2024

DOI: 10.1039/d4ta04290e

rsc.li/materials-a

Introduction

The increasing demand for energy and the requirement to reduce environmental costs urgently necessitate the development of a new clean energy source. Thermoelectric (TE) technology, renowned for its cleanliness, stability, and silent operation, has garnered significant attention as a potential means for directly converting exhaust heat into electrical energy, thereby alleviating global energy challenges and reducing environmental pollution.[1,2] TE performance is usually evaluated using a dimensionless figure of merit $ZT = S^2\sigma T/\kappa_{tot} = S^2\sigma T/(\kappa_{lat} + \kappa_{ele})$, where S, σ, T, and κ_{tot} are the Seebeck coefficient, electrical conductivity, absolute temperature, and total thermal conductivity contributed by charge carriers (κ_{ele}) and lattice vibrations (κ_{lat}), respectively. Desirable ZT values can be obtained by increasing the power factor ($PF = S^2\sigma$) and reducing the thermal conductivity.[3,4] Over the past few decades, researchers have proposed many successful strategies to improve TE performance. For example, the PF can be improved by regulating the band structure, introducing resonant states,[5,6] energy filtering,[7,8] and suppressing lattice thermal conductivity (κ_{lat}) through anharmonic effects and crystal defect engineering, which includes point defects,[9–11] dislocations,[12–14] nanoprecipitates,[15,16] and hierarchical architectures.[17,18] However, the above strategies are subject to the strong coupling between carrier and phonon transport, making the development of TE materials with high ZT values extremely challenging. PbSe-based TE materials with a rock-salt structure, similar to PbTe, have become ideal candidates due to their low cost, abundant earth reserves,[19] and high mechanical strength.[20] However, n-type PbSe has a large energy gap (above 0.4 eV) between its L and Σ conduction bands and a single electronic conduction band near the Fermi level; these features prevent band convergence and improvement of the PF by chemical doping and alloying.[17,21] Therefore, its TE performance is often improved by intensifying phonon scattering through defect structure design.[15,22]

[a]*Department of Nuclear Science and Technology, Nanjing University of Aeronautics and Astronautics, Nanjing 211106, China*

[b]*Key Laboratory of Nuclear Technology Application and Radiation Protection in Aerospace, Ministry of Industry and Information Technology, Nanjing 211106, China. E-mail: fdchen@nuaa.edu.cn; tangxiaobin@nuaa.edu.cn*

[c]*Interdisciplinary Materials Research Center, School of Materials Science and Engineering, Tongji Univ., 4800 Caoan Rd., Shanghai 201804, China*

[d]*School of Materials Science and Engineering, Liaocheng University, Liaocheng 252059, China*

† Electronic supplementary information (ESI) available. See DOI: https://doi.org/10.1039/d4ta04290e

In PbQ (Q = Te, Se, S) compounds, small-sized Zn, [23,24] Ni,[24] Cu,[12,25–27] and Ag atoms can serve as interstitials in the matrix. Unlike the strong carrier scattering caused by nanostructures, the sub-nanoscale interstitials can achieve decoupling of carrier and phonon transport,[27] which is expected to achieve a high PF and ZT simultaneously. Cu ions have prominent advantages among these small-sized atoms due to their small ion radius (~0.6 Å) and low formation energy, which do not alter the electron scattering mechanism in the PbSe lattice.[25] Limited by the solid solubility of Cu, the introduction of Cu into the matrix often results in the formation of interstitial atoms and second phases, which can dynamically optimize the carrier concentration and reduce lattice thermal conductivity to optimize TE performance with increasing temperature. Promoting the dissolution of second phases will be an effective means to further optimize the dynamic doping effect. Additionally, for a given system, an increase in configurational entropy (ΔS_{conf}) can extend the solubility limits of alloying elements and enhance structural stabilization,[28,29] increasing the band degeneracy and improving the Seebeck coefficient. The high-entropy effect also leads to severe lattice disorder and mass and strain fluctuations, which strengthen phonon scattering and reduce κ_{lat}. [30] According to the Boltzmann principle, the configurational entropy can be expressed as $\Delta S_{conf} = -N_A\kappa_B \sum_{I=1}^{n} x_i \ln x_i$, where κ_B is the Boltzmann constant, x_i is the molar ratio of the ith component, and N_A is Avogadro's constant. By combining multiple principal elements, ΔS_{conf} can be maximized to achieve enhanced performance in TE materials. However, a high ΔS_{conf} can hinder carrier transport, limiting the improvement in thermoelectric performance.[31] Therefore, exploring a synergistic approach that harnesses the entropy effect to drive the dynamic doping effect across a wide temperature range is necessary to achieve high electrical performance and maintain the advantage of low intrinsic thermal conductivity.

In this work, based on different values of ΔS_{conf}, we synthesized a series of entropy-increased n-type lead chalcogenide compounds $Pb_{1-y}Sn_ySe_{1-x}Te_xS_x$-2 at% Cu ($x = 0.1$ and $y = 0$; $x = 0.25$ and $y = 0$; $x = 0.25$ and $y = 0.125$). First, excessive Cu (2at%) interstitial doping was introduced into PbSe to optimize the carrier concentration of the matrix at room temperature and enhance phonon scattering. Te, S, and Sn were introduced to further enhance lattice distortion, resulting in PbSe-based TE materials with low, medium, and high entropy levels. The introduction of Cu significantly increases the carrier concentration of the matrix, and the room-temperature carrier concentration of PbSe-2at%Cu reaches ~3.02×10^{19} cm^{-3}. With the increase in ΔS_{conf}, the room-temperature carrier concentration decreases to ~1.0×10^{18} cm^{-3} in $Pb_{0.875}Sn_{0.125}Se_{0.5}Te_{0.25}S_{0.25}$-2at%Cu. However, the entropy-driven structural stabilization effect leads to an enhanced Seebeck coefficient of -363 μV K^{-1}, maintaining good electrical performance. Meanwhile, dense dislocations, nanoscale to submicron-scale Sn- and Cu-rich incoherent precipitates and severe lattice distortion driven by entropy hinder phonon propagation, enhance anharmonicity, and reduce κ_{lat}. Ultimately, the high-entropy sample $Pb_{0.875}Sn_{0.125}Se_{0.5}Te_{0.25}S_{0.25}$-2at%Cu achieves a ZT value of 0.64 at room temperature and a peak ZT value of 1.46 at 623 K, with a notable average ZT value exceeding 1.15 at 300–700 K.

Results

Crystal characterization and microstructure observation

The XRD patterns of $Pb_{1-y}Sn_ySe_{1-x}Te_xS_x$-2at%Cu ($x = 0$ and $y = 0$; $x = 0.1$ and $y = 0$; $x = 0.25$ and $y = 0$; $x = 0.25$ and $y = 0.125$) samples are shown in Fig. 1a. All the peaks were indexed as belonging to the standard face-centered cubic structure with the $Fm\bar{3}m$ space group, and there was no discernible presence of an impurity phase. With rising Te/S/Sn content, a significant shift of peaks to low angles was observed in the samples, indicating lattice expansion. Notably, when the content of Te and S reached 25at%, the (200) peak tended to split into several peaks.[32] After introducing Sn into the alloy, the split peaks of the high-entropy sample $Pb_{0.875}Sn_{0.125}Se_{0.5}Te_{0.25}S_{0.25}$-2at%Cu converged into a single (200) peak, which showed a typical structural stabilization effect driven by entropy.[32] Furthermore, we performed structural refinement to uncover alterations in lattice parameters (Fig. 1b). The lattice parameters increased with increasing atomic fraction of Te/S/Sn doping. Subsequently, we extracted the full width at half maximum (FWHM) from the XRD data to qualitatively evaluate the lattice disorder degree in the samples. As ΔS_{conf} increased, both the FWHM at the (200) plane and microstrain (ε) exhibited a trend of first increasing and then falling, as shown in Fig. 1c and d. This result may be due to the large amount of lattice distortion introduced by the doping of Te and S into the matrix, whereas the introduction of Sn stabilized the lattice. Notably, as a result of phase separation, the ε value of the $PbTe_{0.25}S_{0.25}Se_{0.5}$-2at%Cu sample reached 0.62%, which was significantly higher than that of existing high-entropy TE materials.[32,33] Although the ε value of the high-entropy sample $Pb_{0.875}Sn_{0.125}Se_{0.5}Te_{0.25}S_{0.25}$-2at%Cu was 0.37%, it reflected the structural stabilization effect driven by the high entropy, which was much lower than that of the medium-entropy sample $PbSe_{0.5}Te_{0.25}S_{0.25}$-2at%Cu.

To analyze the influence of the high-entropy effect on the microstructure of the matrix, we employed transmission electron microscopy (TEM) and scanning transmission electron microscopy (STEM) to observe the detailed structural features in $Pb_{0.875}Sn_{0.125}Se_{0.5}Te_{0.25}S_{0.25}$-2at%Cu. The low- to high-magnification TEM images in Fig. 2a–c present a high density of dislocations and different brightness/contrast in the matrix. Fig. 2e displays an enlarged high-resolution transmission electron microscopy (HRTEM) image in the inset of Fig. 2d located in a dislocation-free region. Fig. 2f shows an inverse fast Fourier transform (IFFT) image that provides a clear depiction of the dislocation. Abundant lattice distortions can also be observed in many gray blurred areas. All the figures confirmed that a large number of dislocations and lattice distortions effectively contribute to the deterioration of thermal properties.

The STEM images of the $Pb_{0.875}Sn_{0.125}Se_{0.5}Te_{0.25}S_{0.25}$-2at%Cu sample reveal nanoscale to submicron-scale incoherent precipitates in the matrix (Fig. 3). The STEM images in Fig. 3a illustrate the micromorphology of rod-shaped and elliptical-shaped

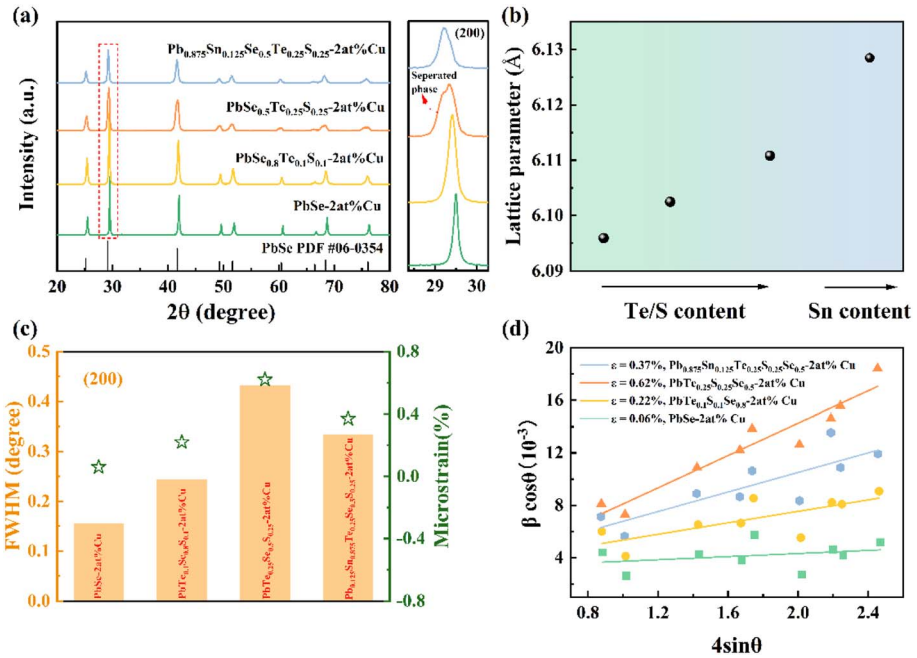

Fig. 1 X-ray diffraction patterns and strain analysis of $Pb_{1-y}Sn_ySe_{1-x}Te_xS_x$-2at%Cu ($x = 0$ and $y = 0$; $x = 0.1$ and $y = 0$; $x = 0.25$ and $y = 0$; $x = 0.25$ and $y = 0.125$) samples: (a) X-ray diffraction patterns. (b) Lattice parameter. (c) Full width at half maximum (FWHM) at the (200) peak and microstrain (ε). (d) microstrain (ε) estimated from the Williamson–Hall plot.

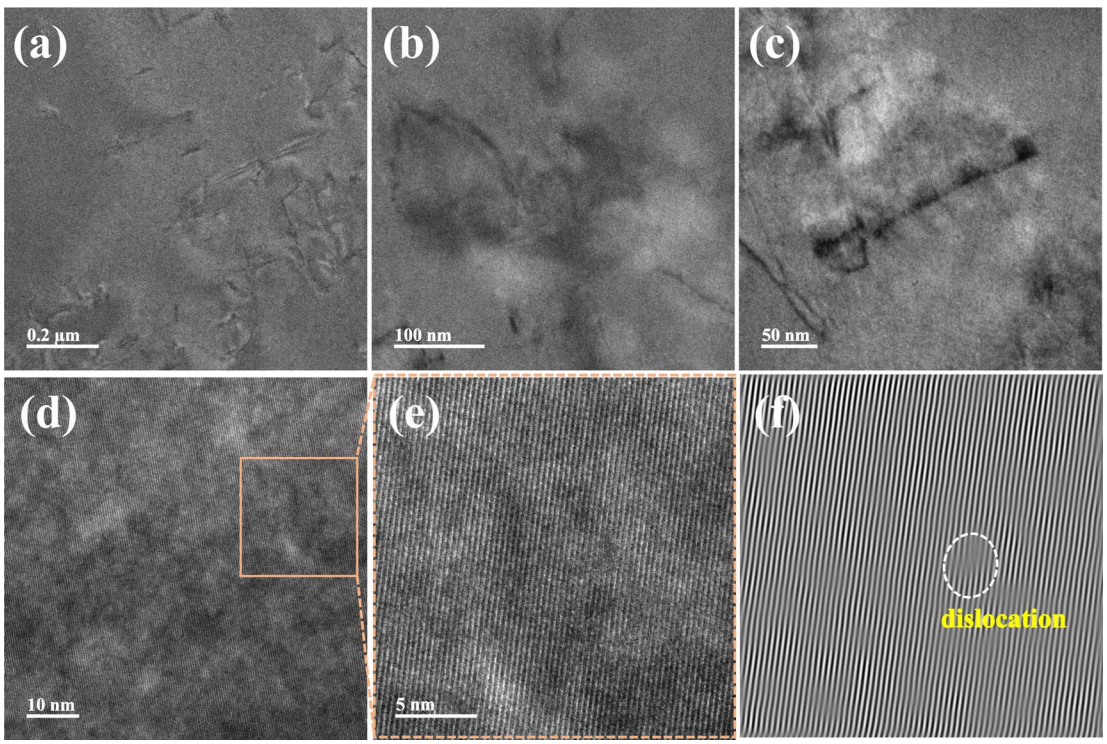

Fig. 2 Microstructure observation in the $Pb_{0.875}Sn_{0.125}Se_{0.5}Te_{0.25}S_{0.25}$-2at%Cu sample by TEM: (a–c) low- to high-magnification images showing dense linear defects in the PbSe matrix. (d and e) HRTEM image of the other region. (f) Corresponding FFT image of the enlarged region of (e).

precipitates. To identify the composition, we performed EDS analysis for the rod-shaped precipitates, and the results are depicted in Fig. 3b–g. The Sn element and Cu element were highly concentrated in the precipitate, which indicated that the amount of Cu may exceed the solid solubility limit of $Pb_{0.875}Sn_{0.125}Se_{0.5}Te_{0.25}S_{0.25}$-2at%Cu, resulting in the formation of Sn-

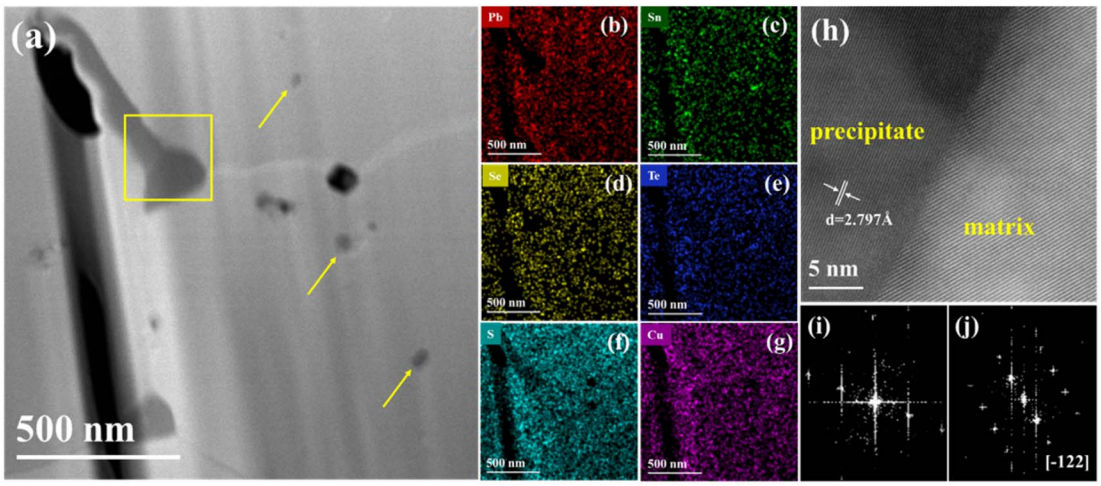

Fig. 3 Microstructure observation of $Pb_{0.875}Sn_{0.125}Se_{0.5}Te_{0.25}S_{0.25}$-2at%Cu samples by STEM: (a) the low-magnification microscopic morphological image; (b–g) respective EDS mappings of Pb, Sn, Se, Te, S, and Cu; (h) high-angle annular dark field (HAADF) image of the incoherent interface for the rod-shaped precipitate; (i) high-angle angular dark field (HAADF) image of the rod-shaped precipitate; (j) IFFT images of (h) in the precipitate and matrix, respectively.

and Cu-rich precipitates. Fig. 3h presents an atomic-resolution high-angle annular dark field (HAADF) image of the incoherent interface for the rod-shaped precipitate in Fig. 3a, which was imaged under the [013] zone axis of the matrix. The fast Fourier transform (FFT) image shown in Fig. 3j was obtained at the incoherent interface. The interplanar spacing along [200] of the matrix was 3.22 Å, and the calculated lattice constant was approximately 6.44 Å, which was close to the lattice constant obtained through XRD, both indicating a significant expansion of the matrix lattice of $Pb_{0.875}Sn_{0.125}Se_{0.5}Te_{0.25}S_{0.25}$ compared with PbSe. Given that the precipitates were tilted off the zone axis, the specific structure of these precipitates has not been identified. The Sn- and Cu-rich precipitates were incoherent with the matrix,[34] which may exhibit a different behavior from Cu_2Se,

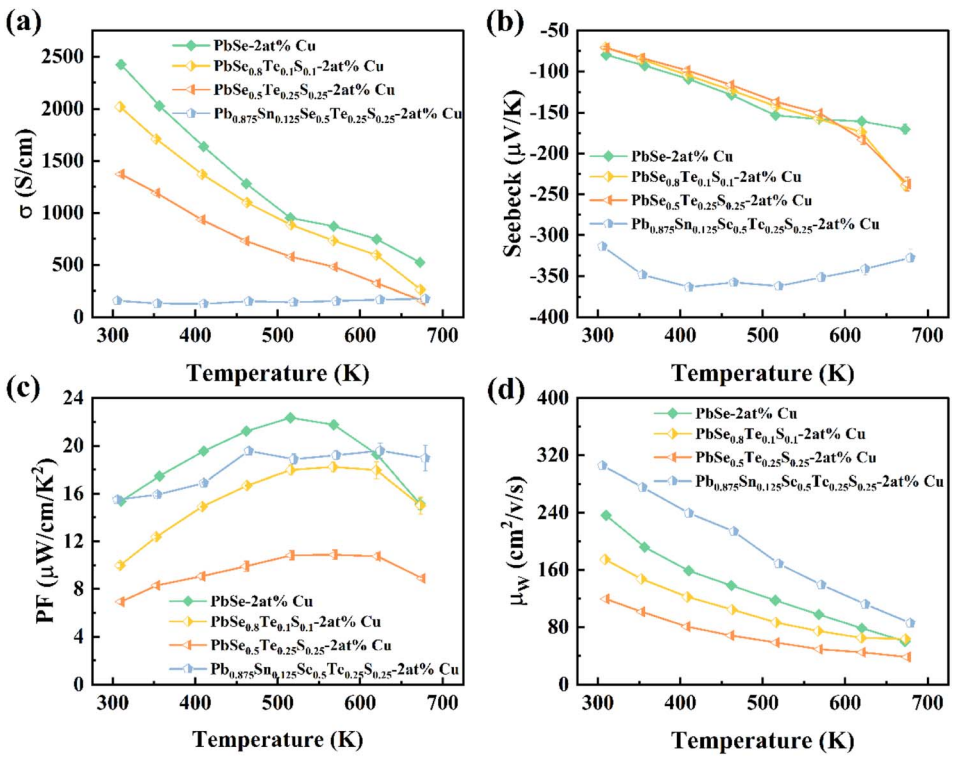

Fig. 4 Temperature-dependent electrical transport properties of $Pb_{1-y}Sn_ySe_{1-x}Te_xS_x$-2at%Cu ($x = 0$ and $y = 0$; $x = 0.1$ and $y = 0$; $x = 0.25$ and $y = 0$; $x = 0.25$ and $y = 0.125$) samples: (a) electrical conductivity, σ; (b) Seebeck coefficient, S; (c) power factor, PF; and (d) weighted carrier mobility (μ_w).

adding complexity and richness to the microstructure of $Pb_{0.875}Sn_{0.125}Se_{0.5}Te_{0.25}S_{0.25}$-2at%Cu and strongly intensifying phonon scattering.

Charge transport properties

Fig. 4 demonstrates the electrical transport properties of $Pb_{1-y}Sn_ySe_{1-x}Te_xS_x$-2at%Cu ($x = 0$ and $y = 0$; $x = 0.1$ and $y = 0$; $x = 0.25$ and $y = 0$; $x = 0.25$ and $y = 0.125$) samples as a function of temperature. As depicted in Fig. 4a, with the increase in ΔS_{conf}, the electrical conductivity (σ) of all samples gradually decreased, which may be due to the deterioration of charge transport caused by the entropy-driven disorder.[31,35] All samples demonstrated a negative Seebeck coefficient (S), indicating the n-type TE material classification, as depicted in Fig. 4b. The S of the entropy-increasing system exhibited a trend opposite to σ, and the $|S|$ of the high-entropy sample $Pb_{0.875}Sn_{0.125}Se_{0.5}Te_{0.25}S_{0.25}$-2at%Cu increased to 363.4 μV K^{-1}. Notably, the significant enhancement in S compensated for the decrease in σ. Ultimately, the PF reached 19.5 μW cm^{-1} K^{-2} in $Pb_{0.875}Sn_{0.125}Se_{0.5}Te_{0.25}S_{0.25}$-2at%Cu, which may be attributed to the structural stabilization effect maintained under the influence of entropy, contributing to good electrical properties. The weighted mobility (μ_w), such as hall mobility (μ_H), can be defined as a simple function of S and σ to quantitatively measure the electron transport properties of TE materials.[36] Here, μ_w is introduced to evaluate the contribution of ΔS_{conf}. Based on the free electron (parabolic band) Drude–Sommerfeld model, μ_w can be calculated using eqn (1)–(3):[37]

$$\mu_w = \frac{3\sigma}{8\pi e F_0(\eta)}\left(\frac{h^2}{2m_e k_B T}\right)^{3/2} \quad (1)$$

$$F_0(\eta) = \int_0^\infty \frac{\chi^n}{1+e^{\chi-\eta}}\mathrm{d}\chi \quad (2)$$

$$S = \pm\frac{\kappa_B}{e}\left(\frac{\left(r+\frac{5}{2}\right)F_{r+\frac{3}{2}}(\eta)}{\left(r+\frac{3}{2}\right)F_{r+\frac{1}{2}}(\eta)} - \eta\right) \quad (3)$$

where e, h, m_e, and κ_B represent the united charge, the Planck constant, the electron mass, and the Boltzmann constant, respectively. $F_n(\eta)$ denotes the Fermi integral, η denotes the reduced Fermi level, and r denotes the scattering factor, which equals −1/2 when acoustic scattering is the dominant mechanism. Owing to the limitation of the scattering mechanism considered by the model, especially for high-entropy samples with low carrier concentration, the μ_w of the high-entropy sample was overestimated.[37,38] However, we can still utilize its changing trend to validate the electrical properties. According to the temperature-dependent curve of μ_w (Fig. 4d), the μ_w of the high-entropy sample $Pb_{0.875}Sn_{0.125}Se_{0.5}Te_{0.25}S_{0.25}$-2at%Cu remarkably improved, reaching a maximum value of 305.66 cm^2 V^{-1} s^{-1} at room temperature, which also demonstrated why the high-entropy effect enhanced electrical properties.

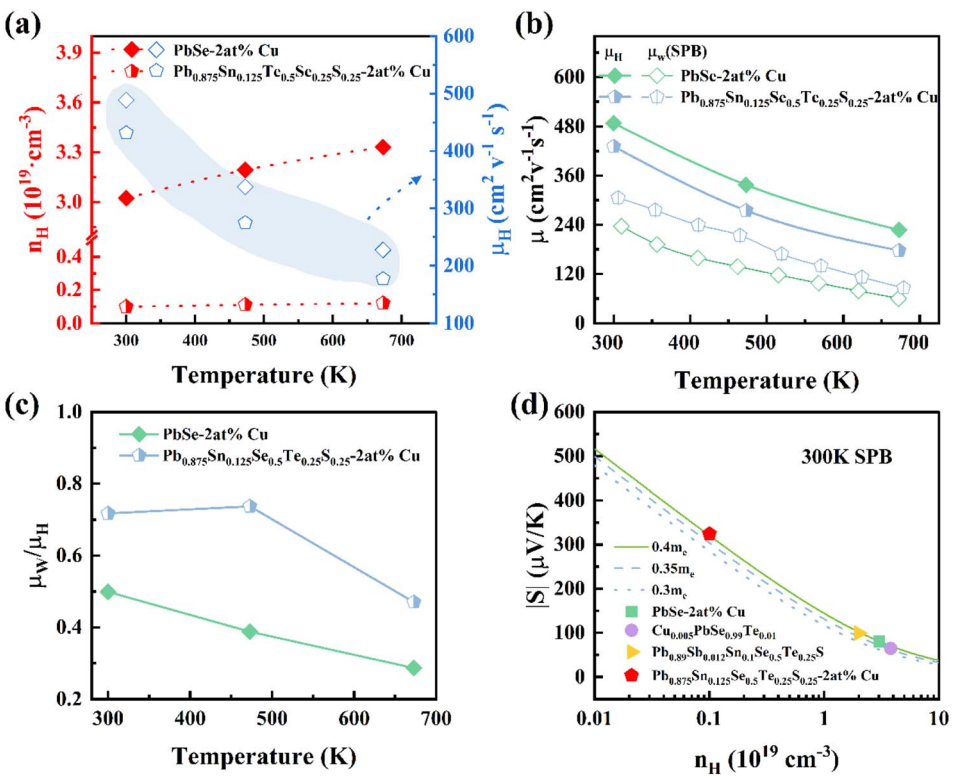

Fig. 5 Charge transport properties of PbSe-2at%Cu and $Pb_{0.875}Sn_{0.125}Se_{0.5}Te_{0.25}S_{0.25}$-2at%Cu: (a) carrier concentration (n_H) and carrier mobility (μ_H); (b) comparison of μ_w and μ_H; (c) μ_w/μ_H for PbSe-2at%Cu and $Pb_{0.875}Sn_{0.125}Se_{0.5}Te_{0.25}S_{0.25}$-2at%Cu.

To reveal the electrical transport properties of the samples driven by entropy, we performed variable-temperature hall effect measurements on the low-entropy sample PbSe-2at%Cu and the high-entropy sample $Pb_{0.875}Sn_{0.125}Se_{0.5}Te_{0.25}S_{0.25}$-2at%Cu, as shown in Fig. 5. Fig. 5a depicts the variation in carrier concentration (n_H) and carrier mobility (μ_H) for the samples. The n_H of PbSe-2at%Cu increased with rising temperature, reflecting the dynamic optimization of carriers under Cu doping. Although Cu doping optimized the n_H and μ_H of PbSe, the room-temperature μ_H decreased from 488.2 $cm^2\ v^{-1}\ s^{-1}$ for PbSe-2at%Cu to 431.5 $cm^2\ v^{-1}\ s^{-1}$ for $Pb_{0.875}Sn_{0.125}Se_{0.5}Te_{0.25}S_{0.25}$-2at%Cu. Compared to previously reported single-doped and co-doped alloys,[39] high-entropy alloys typically have a lower μ due to the intensified alloying scattering of charge carriers.[29] Subsequently, we quantitatively estimated the effective mass (m^*) to assess the changes in the band structure driven by entropy. μ_w is proportional to m^* according to eqn (4):[40,41]

$$\mu_w \approx \mu_H \left(\frac{m^*}{m_e}\right)^{3/2} \quad (4)$$

where μ_H refers to the hall carrier mobility, μ_w is the weighted carrier mobility, and m_e is the free electron mass. The above m^* signifies a calculated value, commonly referred to as the Seebeck coefficient mass (m_S^*), which can be ascertained through S and its corresponding n_H.[42] Fig. 5b compares the μ_w and μ_H of the samples as a function of temperature. The deviation between the μ_w and μ_H of the samples increased significantly with the increase in ΔS_{conf}. The μ_w/μ_H values in Fig. 5c also demonstrated this enhanced deviation, quantitatively illustrating the increase in m^* under high entropy.

The single parabolic band (SPB) model is employed to investigate the influence of high entropy on the band structure. Pisarenko curves [43,44] with different DOS effective masses (m^*) at 300 K for PbSe-2at%Cu and $Pb_{0.875}Sn_{0.125}Se_{0.5}Te_{0.25}S_{0.25}$-2at%Cu are theoretically plotted in Fig. 5d. The solid and dashed lines represent theoretical values based on the SPB model assuming that the m^* of PbSe is 0.3 m_e, 0.35 m_e and 0.4 m_e, respectively. The experimental values of PbSe-2at%Cu and $Pb_{0.875}Sn_{0.125}Se_{0.5}Te_{0.25}S_{0.25}$-2at%Cu fell around the green solid line with $m^* = 0.4\ m_e$, in which m^* gradually increased with high values of 0.34 m_e and 0.41 m_e achieved in PbSe-2at%Cu and $Pb_{0.875}Sn_{0.125}Se_{0.5}Te_{0.25}S_{0.25}$-2at%Cu, respectively. This serves as a crucial aspect for enhancing $|S|$ across the entire temperature range. Upon comparison, the m^* of $Pb_{0.875}Sn_{0.125}Se_{0.5}Te_{0.25}S_{0.25}$-2at%Cu even exceeded those of $Cu_{0.005}PbSe_{0.99}Te_{0.01}$ (ref. 26) and $Pb_{0.89}Sb_{0.012}Sn_{0.1}Se_{0.5}Te_{0.25}S_{0.25}$ (ref. 32).

Thermal transport properties and *ZT* value

The temperature-dependent thermal transport properties of all samples, including total thermal conductivity (κ_{tot}) and lattice thermal conductivity (κ_{lat}), are shown in Fig. 6a and b. As expected, entropy engineering plays a major role in the reduction of thermal conductivity. As ΔS_{conf} increased, the κ_{tot} of the samples monotonically decreased. Notably, the κ_{tot} of the samples decreased from 2.65 $W\ m^{-1}\ K^{-1}$ for PbSe-2at%Cu to 0.80 $W\ m^{-1}\ K^{-1}$ for $Pb_{0.875}Sn_{0.125}Se_{0.5}Te_{0.25}S_{0.25}$-2at%Cu at room temperature.

According to Fig. 6b, although the κ_{lat} of the entropy-increasing samples did not significantly decrease due to lattice disorder, which may be due to the decrease in κ_{ele} (Fig. S1, ESI†) under strong alloy scattering, the κ_{lat} of $Pb_{0.875}Sn_{0.125}Se_{0.5}Te_{0.25}S_{0.25}$-2at%Cu still decreased to 0.73 $W\ m^{-1}\ K^{-1}$ at room temperature.

To evaluate the synergistic effect of ΔS_{conf} on the TE transport properties, we first calculated the ratio of μ_w to the lattice thermal conductivity (μ_w/κ_{lat}) as a function of temperature (Fig. 7a). μ_w/κ_{lat} initially decreased and then increased with increasing ΔS_{conf}, with the high-entropy sample $Pb_{0.875}Sn_{0.125}Se_{0.5}Te_{0.25}S_{0.25}$-2at%Cu exhibiting a significant enhancement. This result indicated that the entropy-driven disorder simultaneously optimized charge and phonon properties. Consequently, the *ZT* value of the high-entropy sample $Pb_{0.875}Sn_{0.125}Se_{0.5}Te_{0.25}S_{0.25}$-2at%Cu significantly increased (Fig. 7b), resulting in a *ZT* value of ~0.64 at room temperature and ~1.46 at 623 K.

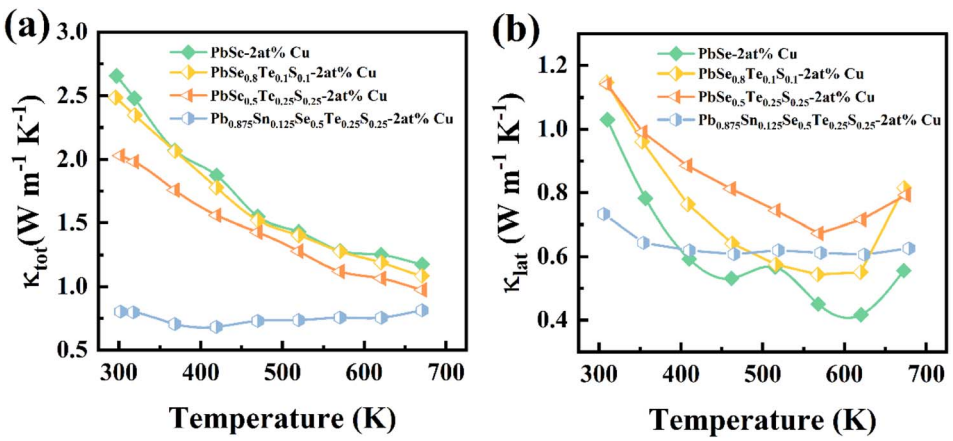

Fig. 6 Temperature-dependent thermal properties of $Pb_{1-y}Sn_ySe_{1-x}Te_xS_x$-2at%Cu ($x = 0$ and $y = 0$; $x = 0.1$ and $y = 0$; $x = 0.25$ and $y = 0$; $x = 0.25$ and $y = 0.125$) samples: (a) total thermal conductivity, κ_{tot}; (b) lattice thermal conductivity, κ_{lat}.

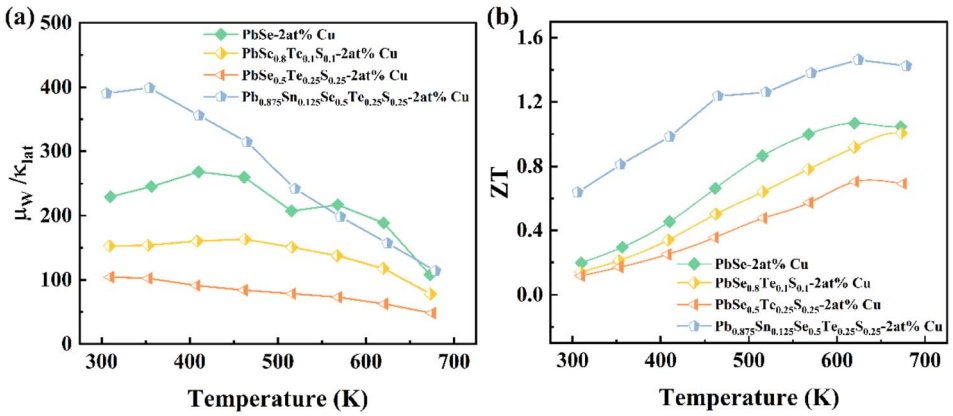

Fig. 7 Temperature-dependent thermoelectric properties of $Pb_{1-y}Sn_ySe_{1-x}Te_xS_x$-2at%Cu ($x = 0$ and $y = 0$; $x = 0.1$ and $y = 0$; $x = 0.25$ and $y = 0$; $x = 0.25$ and $y = 0.125$) samples: (a) ratio of weighted carrier mobility to lattice thermal conductivity; (b) *ZT*.

Discussion

Influence of entropy on charge and phonon transport

As previously mentioned, ΔS_{conf} strongly affects electron and phonon transport properties. In general, the increase in ΔS_{conf} could enhance the solid solubility of the matrix, thereby increasing Cu interstitial doping and optimizing the n_H of $Pb_{1-y}Sn_ySe_{1-x}Te_xS_x$-2at%Cu ($x = 0$ and $y = 0$; $x = 0.1$, 0.25 and $y = 0$; $x = 0.25$ and $y = 0.125$) samples. However, in practice, as the number of elements increased, the disorder and impurities present in the lattice strongly scattered charge carriers, leading to a decrease in n_H and μ_H from 488.2 $cm^2\ V^{-1}\ s^{-1}$ for PbSe-2at%Cu to 431.5 $cm^2\ V^{-1}\ s^{-1}$ for $Pb_{0.875}Sn_{0.125}Se_{0.5}Te_{0.25}S_{0.25}$-2at%Cu.

To further investigate the microscopic mechanism behind this performance change of $Pb_{1-y}Sn_ySe_{1-x}Te_xS_x$-2at%Cu ($x = 0$ and $y = 0$; $x = 0.1$ and $y = 0$; $x = 0.25$ and $y = 0$; $x = 0.25$ and $y = 0.125$) samples, we conducted positron annihilation lifetime (PAL) measurements. Following the deduction of source and background components, all lifetime spectra could be dissected into three lifetime components, namely, τ_1, τ_2, and τ_3, using the LT9 program. I_1, I_2, and I_3 denote the corresponding intensities of τ_1, τ_2, and τ_3, respectively. The average lifetime (τ_{ave}) of all samples was calculated using $\tau_{ave} = \tau_1 I_1 + \tau_2 I_2 + \tau_3 I_3$. All positron lifetime results are shown in Fig. 8. Krause[45] *et al.* and Polity[46] *et al.* reported that the calculated positron lifetimes in the PbSe bulk state (τ_b) and at Pb vacancies ($\tau_{V_{Pb}}$) are 213 and 298 ps, respectively. Therefore, τ_1 is the bulk lifetime; τ_2 is the positron lifetime trapped at Pb vacancy defects; and τ_3 is the positron lifetime at the grain surface, large pores, and internal interface defects. Fig. 8a and b display the PAL experimental spectra and fitting curves for PbSe-2at%Cu and $Pb_{0.875}Sn_{0.125}Se_{0.5}Te_{0.25}S_{0.25}$-2at%Cu, respectively. As ΔS_{conf} increased, τ_1 increased linearly from 190 ps for PbSe-2at%Cu to 290 ps for $Pb_{0.875}Sn_{0.125}Se_{0.5}Te_{0.25}S_{0.25}$-2at%Cu (Fig. 8c). This result suggested a decrease in the charge concentration of the PbSe matrix, which was consistent with the decrease in n_H from 3.02×10^{19} cm^{-3} to 1.0×10^{18} cm^{-3}, as well as a change in σ. τ_2 increased from 300 ps

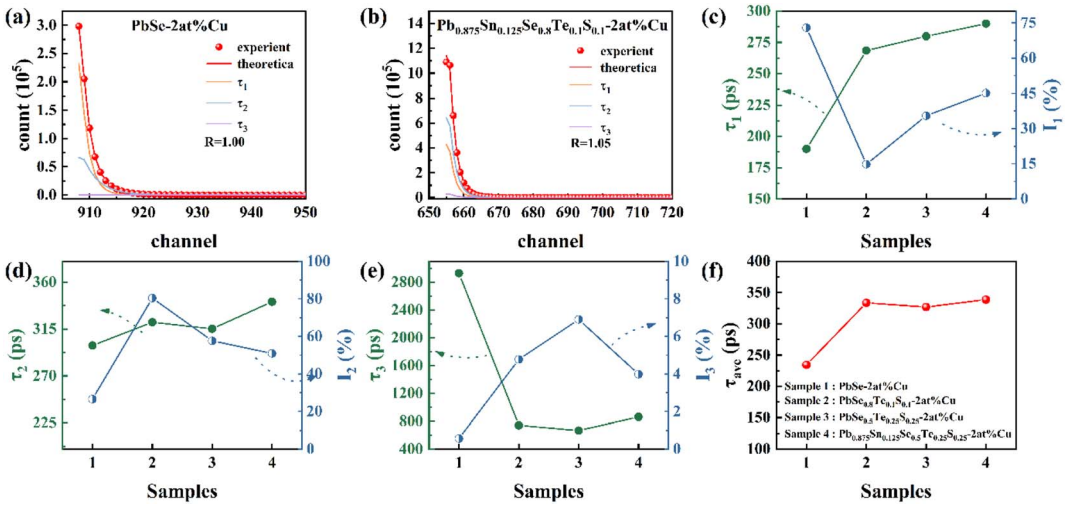

Fig. 8 Positron annihilation lifetime of $Pb_{1-y}Sn_ySe_{1-x}Te_xS_x$-2at%Cu ($x = 0$ and $y = 0$; $x = 0.1$ and $y = 0$; $x = 0.25$ and $y = 0$; $x = 0.25$ and $y = 0.125$) samples: (a) and (b) positron annihilation lifetime experimental spectra and fitting curves; (c) τ_1 and I_1; (d) τ_2 and I_2; (e) τ_3 and I_3; (f) τ_{ave}.

to 350 ps in Fig. 8d, indicating that the size of the vacancy defects increased, and the Pb monovacancy transformed into a Pb–Sn divacancy with increasing ΔS_{conf}.[45] Additionally, the calculated τ_{ave} increased from 234.4 ps to 338.7 ps in Fig. 8f, indicating a decrease in electron concentration and an increase in defect types within the matrix.

Notably, n_H in the low-entropy sample PbSe-2at%Cu increased with rising temperature, which was consistent with the phenomenon observed in Cu-doped samples,[24,25,47–49] where Cu-rich precipitates present in the matrix dissolved upon temperature elevation, resulting in an enhancement of n_H in the matrix. However, n_H in $Pb_{0.875}Sn_{0.125}Se_{0.5}Te_{0.25}S_{0.25}$-2at%Cu remained nearly unchanged over the entire temperature range, indicating poor electron doping efficiency. Different from the common Cu precipitates, the precipitates in $Pb_{0.875}Sn_{0.125}Se_{0.5}Te_{0.25}S_{0.25}$-2at%Cu were composed of Cu element and Sn element. The nanoscale to submicron-scale incoherent phases resulted from the precipitation of Cu, which may not dissolve to achieve carrier optimization under variable temperatures, thereby reducing the content of Cu interstitials and decreasing n_H. To prove the doping effect of Cu on the electrical transport properties of the high-entropy sample, we prepared a sample without Cu ($Pb_{0.875}Sn_{0.125}Se_{0.5}Te_{0.25}S_{0.25}$). Its σ value at room temperature was significantly lower than that of $Pb_{0.875}Sn_{0.125}Se_{0.5}Te_{0.25}S_{0.25}$-2at%Cu, which indicated that the introduction of Cu still provided carriers for the matrix. This difference in the second phase led to a variance in the dynamic doping behavior of Cu ions in the high-entropy sample. Given the difference in the second phase, the dynamic doping effect cannot be directly compared through changes in ΔS_{conf}, and a specific analysis of the evolution behavior of the second phases in the matrix is required.

Additionally, m^* exhibited significant differences between PbSe-2at%Cu and $Pb_{0.875}Sn_{0.125}Se_{0.5}Te_{0.25}S_{0.25}$-2at%Cu. The enhancement in m^* indicated the variation in the energy band structure, which was closely related to the high symmetry structure and altered orbital hybridization induced by entropy engineering.[50] In general, materials with high symmetry are anticipated to generate many equivalent positions in reciprocal space, ultimately resulting in the convergence of multiple electronic bands near the Fermi level. Here, we performed first-principles density functional theory calculations, as shown in Fig. 9. Fig. 9a and b demonstrate the established unit cell structures of low-entropy PbSe and high-entropy PbSe. As shown in Fig. 9c and d, a large number of impurity bands appeared in the conduction and valence bands due to the introduction of Se/Te/Sn. Multiple energy bands pushed the peak of the band toward the Fermi level, reducing an energy difference between different energy valleys and enhancing the band degeneracy N_V. The band gap (E_g) decreased, which is consistent with the experimental results of the optical band gap (Fig. S2†). As shown in Fig. 9e, the high-entropy sample exhibited a significant increase in the DOS near the Fermi level compared with the low-entropy sample, which will exhibit an effect of electronic resonance states. The improvement of the resonance density of electrons will strongly scatter the carriers, resulting in the deterioration of σ. On the basis of the calculated band structure, the structural stabilization effect driven by high entropy, the convergence of energy bands caused by a large number of impurity energy levels, and the increased DOS near the Fermi level all helped enhance m^* in $Pb_{0.875}Sn_{0.125}Se_{0.5}Te_{0.25}S_{0.25}$-2at%Cu.

In terms of thermal performance, as ΔS_{conf} increased, κ_{tot} was strongly suppressed, which was mainly caused by the strengthened local lattice disorder hindering phonon transport. Meanwhile, the dislocations and the nanoscale to submicron-scale incoherent precipitates presented severe phonon scattering. Similarly, the increase in positron lifetime τ_2 for $Pb_{0.875}Sn_{0.125}Se_{0.5}Te_{0.25}S_{0.25}$-2at%Cu with the increase in ΔS_{conf} could be attributed to the proliferation of defect types in the matrix, contributing to enhanced phonon scattering and reduced thermal conductivity. In conclusion, κ_{lat} decreased

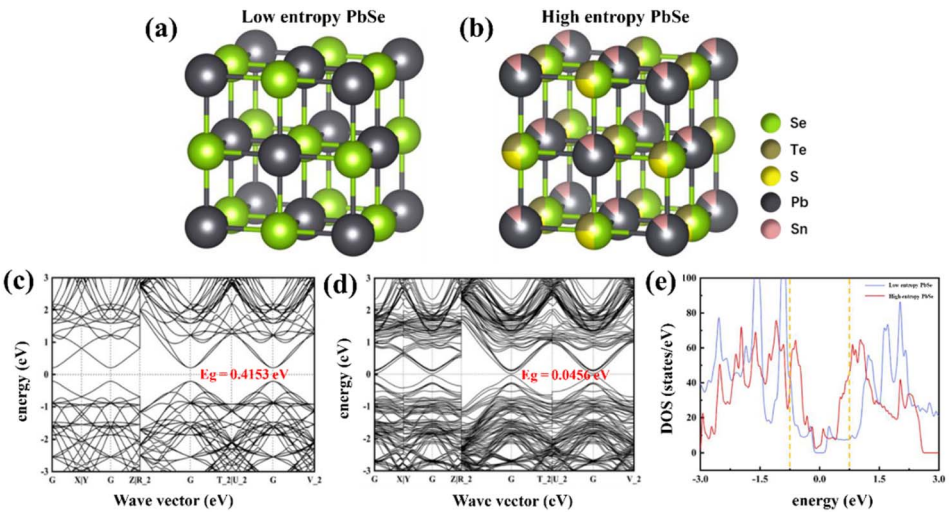

Fig. 9 Cell structure of low-entropy PbSe (a) and high-entropy PbSe (b); (c) calculated electronic band structures for the low-entropy sample and (d) the high-entropy sample; (e) calculated density of states. Their calculated E_g at the conduction band edge is given.

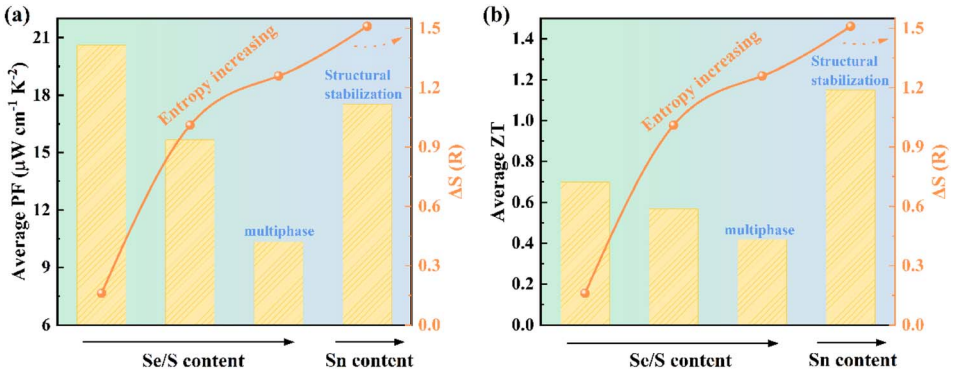

Fig. 10 Thermoelectric properties depending on ΔS_{conf} for $Pb_{1-y}Sn_ySe_{1-x}Te_xS_x$-2at%Cu ($x = 0$ and $y = 0$; $x = 0.1$ and $y = 0$; $x = 0.25$ and $y = 0$; $x = 0.25$ and $y = 0.125$) samples: (a) average PF and (b) average *ZT*.

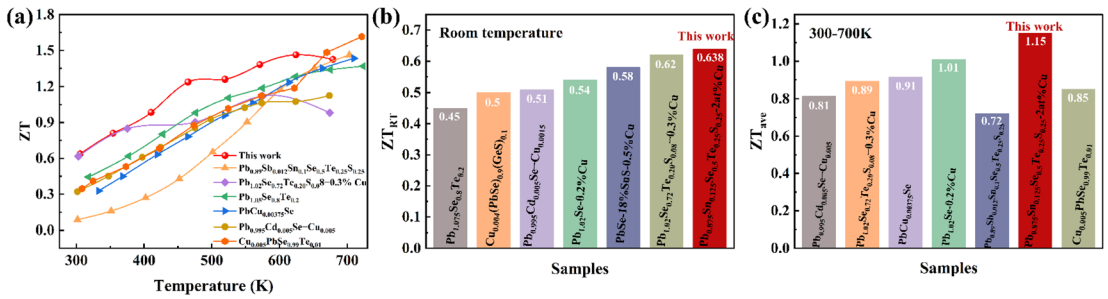

Fig. 11 Comparison of the performance of the high-entropy sample $Pb_{0.875}Sn_{0.125}Se_{0.5}Te_{0.25}S_{0.25}$-2at%Cu in this work with that of reported excellent thermoelectric materials. (a) *ZT*; (b) room temperature *ZT*; (c) average *ZT* between 300 and 700 K.

from 1.03 W m^{-1} K^{-1} to 0.73 W m^{-1} K^{-1} with a drop of 29% at 300 K, whereas κ_{tot} decreased from 2.65 W m^{-1} K^{-1} to 0.80 W m^{-1} K^{-1} with a drop of 69.8%.

Influence of entropy on TE performance

As previously mentioned, ΔS_{conf} strongly affected electron and phonon transport properties. The average PF and average *ZT* *versus* the change in ΔS_{conf} for all samples are shown in Fig. 10a and b. The PF and *ZT* exhibited a similar variation tendency to ΔS_{conf}. Severe alloy scattering in the matrix had a major impact on electrical properties, but the structural stabilization effect of high entropy partially mitigated this adverse effect, restoring electrical performance. Moreover, multiscale defect structures present in the matrix combined with strong lattice disorder driven by high entropy helped enhance phonon scattering, leading to an improvement in the TE performance of the high-entropy sample $Pb_{0.875}Sn_{0.125}Se_{0.5}Te_{0.25}S_{0.25}$-2at%Cu.

In summary, we compare the optimized *ZT* value of the high-entropy sample $Pb_{0.875}Sn_{0.125}Se_{0.5}Te_{0.25}S_{0.25}$-2at%Cu in this work with those of other reported n-type PbSe-based TE materials,[12,25–27,32,51–53] as shown in Fig. 11. The *ZT* value of $Pb_{0.875}Sn_{0.125}Se_{0.5}Te_{0.25}S_{0.25}$-2at%Cu reaches ~0.64 at room temperature, which is superior to those of existing materials, and the average *ZT* value is relatively high. This result demonstrates the feasibility of the optimization method in this work for improving the performance of PbSe-based TE materials.

Conclusions

This study introduced an approach to enhance the TE performance of n-type PbSe materials by using a series of entropy-increased n-type lead chalcogenide compounds $Pb_{1-y}Sn_ySe_{1-x}Te_xS_x$-2at%Cu ($x = 0$ and $y = 0$; $x = 0.1$ and $y = 0$; $x = 0.25$ and $y = 0$; $x = 0.25$ and $y = 0.125$). By gradually increasing alloying to enhance the configurational entropy of PbSe, the introduction of Sn stabilized the lattice of the matrix and promoted the stability of the crystal structure. However, excessive Sn generates Sn- and Cu-rich precipitates, affecting the dynamic doping effect of Cu in PbSe. Thus, the carrier concentration and carrier mobility of $Pb_{0.875}Sn_{0.125}Se_{0.5}Te_{0.25}S_{0.25}$-2at%Cu decreased, leading to low electrical conductivity. Meanwhile, the structural stabilization effect of high entropy increased the effective mass of the electrons, leading to an improved Seebeck coefficient and maintaining a relatively good PF (~19.5 μ W cm^{-1} K^{-2}). The dense dislocations, nanoscale to submicron-scale incoherent precipitates, and large amounts of lattice distortion driven by entropy enhanced phonon scattering and significantly reduced thermal conductivity (~0.80 W m^{-1} K^{-1}). Consequently, an excellent room-temperature *ZT* of ~0.64 (300 K), a peak *ZT* of ~1.46 (623 K), and an average *ZT* of ~1.15 (300–700 K) were achieved in $Pb_{0.875}Sn_{0.125}Se_{0.5}Te_{0.25}S_{0.25}$-2at%Cu. The introduction of Sn could not fully decouple carrier transport and phonon transport. The idea of utilizing the high-entropy effect to enhance Cu dynamic doping is reasonable. To further

enhance the dynamic doping optimization of the high-entropy system, the following possibilities can be considered: (1) adjusting the doping amount of Sn to reduce the generation of precipitates; and (2) combining with elements similar to Sb/Bi to further increase the solid solubility of the matrix and improve the carrier concentration.

Experimental

Experimental preparation

High-purity Cu (99.99%, foil, Macklin), Pb (99.999%, particles, Macklin), Sn (99.999%, particles, Macklin), Se (99.999%, blocks, Macklin), Te (99.999%, particles, Macklin), and S (99.99%, blocks, Macklin) were weighed according to the nominal composition $Pb_{1-y}Sn_ySe_{1-x}Te_xS_x$-2at%Cu ($x = 0$ and $y = 0$; $x = 0.1$ and $y = 0$; $x = 0.25$ and $y = 0$; $x = 0.25$ and $y = 0.125$) and placed into quartz tubes, which were flame-sealed under a dynamic vacuum of $< 5 \times 10^{-3}$ Pa. The vacuum-sealed quartz tube was heated to 1423 K within 14 h, held for 8 h, and cooled to room temperature with a furnace. Thereafter, the ingots were annealed at 873 K for 24 h. The obtained products were hand-ground in an agate mortar for 15 min to a fine powder and then sintered at 823 K under a uniaxial pressure of 50 MPa for 20 min to form dense cylinders with a diameter of 12.5 mm using a fast-hot-pressing furnace (FHP-828). The obtained samples all achieved a relative density of over 98%.

Phase identification and measurement of performance

XRD patterns for all samples were collected on a Rigaku D/max-2200 X-ray diffractometer (PANalytical, the Netherlands) equipped with CuK_α radiation. The microstructure of the samples was characterized by scanning electron microscopy (SEM, Scios 2, Czech) and field-emission transmission electron microscopy (Spectra 300). The hot-pressed samples were cut and polished into various shapes and dimensions to measure charge and thermal transport properties. Bar-shaped samples with the dimensions of $\sim 12 \times 3 \times 3$ mm^3 were employed for measuring the Seebeck coefficient and electrical conductivity simultaneously using a CTA-3 instrument under a low-pressure He atmosphere from 300 K to 700 K. Hall effect measurements as a function of temperature were performed on a PMS–9 system from 300 K to 673 K with a reversible 0.5 T magnetic field. The thermal diffusivity (D) of the sample was measured using the Cowan model with pulse correction using a laser thermal conductivity meter (LFA500), whereas the density (ρ) was determined through Archimedes' drainage method. The heat capacity (C_p) was calculated based on the typical values of lead chalcogenides: $C_p(\kappa_B/\text{atom}) = 3.07 + 0.00047 \times (T - 300)$. κ_{ele} was calculated using the Wiedemann–Franz law: $\kappa_{ele} = L\sigma T$, in which L is the Lorenz number calculated using $L = 1.5 + \exp(-|S|/116)$.

Infrared spectroscopy

The infrared diffuse reflectance spectra were collected on a Thermo Fisher 616 FTIR spectrometer in the mid-IR range (4000–400 cm^{-1}) at ambient temperature. Reflectance data were converted to absorption data using the Kubelka–Munk equation.

Electronic band structure calculations

The density of states (DOS) and band structures in this study were calculated using the Vienna *ab initio* simulation package (VASP).[54,55] Given that the band structure is not changed by intercalating Cu,[25] the constructed supercell did not include Cu atoms, which were only used to optimize the carrier concentration of n-type PbSe. Structural relaxation optimization utilizes the Perdew–Burke–Ernzerhof (PBE) revision within the generalized-gradient approximation (GGA) function.[56] For low-entropy lead selenide materials, a $2 \times 2 \times 2$ supercell was established using ATOMSK.[57] For high-entropy materials, the Alloy–Theoretic Automated Toolkit [58] was introduced to construct a $2 \times 2 \times 2$ (64-atom) supercell based on the $Fm\bar{3}m$ space group PbSe primitive cell, which contained 16 Pb atoms, 8 Te atoms, 8 S atoms, 28 Pb atoms, and 4 Sn atoms. The supercell was fully relaxed with an energy cutoff of 500 eV, and the force converged to 1×10^{-2} eV Å^{-1}.

Data availability

The data that support the findings of this study are available from the corresponding author, F. D. Chen, upon reasonable request.

Author contributions

S. J. Wu: methodology, investigation, data curation, formal analysis, and writing – original draft. C. Y. Li: software and DFT calculation. F. D. Chen: supervision, conceptualization, funding acquisition, and writing – review & editing. K. Yang: methodology and writing – review & editing. C. C. Hu: software and DFT calculation. H. H. Huang: software and DFT calculation. W. J. Huang: formal analysis and writing – review & editing. X. L. Zuo: investigation and writing – review & editing. X. B. Tang: supervision, funding acquisition, and writing – review & editing.

Conflicts of interest

There are no conflicts to declare.

Acknowledgements

This work was financially supported by the National Natural Science 361 Foundation of China (Grant No. 12275130). We also acknowledge the Center for Microscopy and Analysis at the Nanjing University of Aeronautics and Astronautics for their support in microstructure observation.

Notes and references

1 G. Tan, L.-D. Zhao and M. G. Kanatzidis, *Chem. Rev.*, 2016, **116**, 12123–12149.
2 X. Shi and L. Chen, *Nat. Mater.*, 2016, **15**, 691–692.

3 L.-D. Zhao, S.-H. Lo, Y. Zhang, H. Sun, G. Tan, C. Uher, C. Wolverton, V. P. Dravid and M. G. Kanatzidis, *Nature*, 2014, **508**, 373–377.
4 B. Qin, D. Wang, X. Liu, Y. Qin, J.-F. Dong, J. Luo, J.-W. Li, W. Liu, G. Tan, X. Tang, J.-F. Li, J. He and L.-D. Zhao, *Science*, 2021, **373**, 556–561.
5 Q. Zhang, H. Wang, W. Liu, H. Wang, B. Yu, Q. Zhang, Z. Tian, G. Ni, S. Lee, K. Esfarjani, G. Chen and Z. Ren, *Energy Environ. Sci.*, 2012, **5**, 5246–5251.
6 J. P. Heremans, V. Jovovic, E. S. Toberer, A. Saramat, K. Kurosaki, A. Charoenphakdee, S. Yamanaka and G. J. Snyder, *Science*, 2008, **321**, 554–557.
7 H.-T. Liu, Q. Sun, Y. Zhong, C.-L. Xia, Y. Chen, X.-L. Shi, Z.-G. Chen and R. Ang, *Mater. Today Phys.*, 2022, **24**, 100677.
8 J. Zhang, D. Wu, D. He, D. Feng, M. Yin, X. Qin and J. He, *Adv. Mater.*, 2017, **29**, 1703148.
9 L. Fu, M. Yin, D. Wu, W. Li, D. Feng, L. Huang and J. He, *Energy Environ. Sci.*, 2017, **10**, 2030–2040.
10 H. Wang, Y. Pei, A. D. LaLonde and G. J. Snyder, *Adv. Mater.*, 2011, **23**, 1366–1370.
11 M. T. Agne, F. R. L. Lange, J. P. Male, K. S. Siegert, H. Volker, C. Poltorak, A. Poitz, T. Siegrist, S. Maier, G. J. Snyder and M. Wuttig, *Matter*, 2021, **4**, 2970–2984.
12 L. Xu, Y. Xiao, S. Wang, B. Cui, D. Wu, X. Ding and L.-D. Zhao, *Nat. Commun.*, 2022, **13**, 6449.
13 Z. Chen, B. Ge, W. Li, S. Lin, J. Shen, Y. Chang, R. Hanus, G. J. Snyder and Y. Pei, *Nat. Commun.*, 2017, **8**, 13828.
14 M. Hong, Z.-G. Chen, S. Matsumura and J. Zou, *Nano Energy*, 2018, **50**, 785–793.
15 Z.-Z. Luo, S. Hao, X. Zhang, X. Hua, S. Cai, G. Tan, T. P. Bailey, R. Ma, C. Uher, C. Wolverton, V. P. Dravid, Q. Yan and M. G. Kanatzidis, *Energy Environ. Sci.*, 2018, **11**, 3220–3230.
16 C. Zhou, Y. Yu, X. Zhang, Y. Cheng, J. Xu, Y. K. Lee, B. Yoo, O. Cojocaru-Mirédin, G. Liu, S.-P. Cho, M. Wuttig, T. Hyeon and I. Chung, *Adv. Funct. Mater.*, 2020, **30**, 1908405.
17 G. Tan, S. Hao, S. Cai, T. P. Bailey, Z. Luo, I. Hadar, C. Uher, V. P. Dravid, C. Wolverton and M. G. Kanatzidis, *J. Am. Chem. Soc.*, 2019, **141**, 4480–4486.
18 W. Huang, F. Chen, S. Wu and X. Tang, *Mater. Today Commun.*, 2024, **38**, 108265.
19 Z. Hu and S. Gao, *Chem. Geol.*, 2008, **253**, 205–221.
20 Y. Zhong, J. Tang, H. Liu, Z. Chen, L. Lin, D. Ren, B. Liu and R. Ang, *ACS Appl. Mater. Interfaces*, 2020, **12**, 49323–49334.
21 C. Zhou and I. Chung, *Coord. Chem. Rev.*, 2020, **421**, 213437.
22 X. Qian, H. Wu, D. Wang, Y. Zhang, J. Wang, G. Wang, L. Zheng, S. J. Pennycook and L.-D. Zhao, *Energy Environ. Sci.*, 2019, **12**, 1969–1978.
23 X. Qian, H. Wu, D. Wang, Y. Zhang, S. J. Pennycook, X. Gao, L. Zheng and L.-D. Zhao, *Mater. Today Phys.*, 2019, **9**, 100102.
24 X. Qian, D. Wang, Y. Zhang, H. Wu, S. J. Pennycook, L. Zheng, P. F. P. Poudeu and L.-D. Zhao, *J. Mater. Chem. A*, 2020, **8**, 5699–5708.
25 L. You, Y. Liu, X. Li, P. Nan, B. Ge, Y. Jiang, P. Luo, S. Pan, Y. Pei, W. Zhang, G. J. Snyder, J. Yang, J. Zhang and J. Luo, *Energy Environ. Sci.*, 2018, **11**, 1848–1858.
26 C. Zhou, Y. Yu, Y.-L. Lee, B. Ge, W. Lu, O. Cojocaru-Mirédin, J. Im, S.-P. Cho, M. Wuttig, Z. Shi and I. Chung, *J. Am. Chem. Soc.*, 2020, **142**, 15172–15186.
27 L. Xu, X. Wang, Y. Wang, Z. Gao, X. Ding and Y. Xiao, *Energy Environ. Sci.*, 2024, **17**, 2018–2027.
28 A. Sarkar, Q. Wang, A. Schiele, M. R. Chellali, S. S. Bhattacharya, D. Wang, T. Brezesinski, H. Hahn, L. Velasco and B. Breitung, *Adv. Mater.*, 2019, **31**, 1806236.
29 L. Hu, Y. Zhang, H. Wu, J. Li, Y. Li, M. Mckenna, J. He, F. Liu, S. J. Pennycook and X. Zeng, *Adv. Energy Mater.*, 2018, **8**, 1802116.
30 S. Zhi, J. Li, L. Hu, J. Li, N. Li, H. Wu, F. Liu, C. Zhang, W. Ao, H. Xie, X. Zhao, S. J. Pennycook and T. Zhu, *Advanced Science*, 2021, **8**, 2100220.
31 B. Jiang, W. Wang, S. Liu, Y. Wang, C. Wang, Y. Chen, L. Xie, M. Huang and J. He, *Science*, 2022, **377**, 208–213.
32 B. Jiang, Y. Yu, J. Cui, X. Liu, L. Xie, J. Liao, Q. Zhang, Y. Huang, S. Ning, B. Jia, B. Zhu, S. Bai, L. Chen, S. J. Pennycook and J. He, *Science*, 2021, **371**, 830–834.
33 Z. Yuan, M. Wu, S. Han, P.-F. Liu, Z.-H. Ge, B. Ge, M. Zhu, Y. Xu, W. Jie, D. Zhao, B. Yang, Y. Zhang, M. Liu, M. Zhu, C. Li, Y. Yu and C. Zhou, *Energy Environ. Sci.*, 2024, **17**, 2921–2934.
34 S. Liu, Y. Yu, D. Wu, X. Xu, L. Xie, X. Chao, M. Bosman, S. J. Pennycook, Z. Yang and J. He, *Adv. Funct. Mater.*, 2021, **31**, 2007340.
35 S. Roychowdhury, T. Ghosh, R. Arora, M. Samanta, L. Xie, N. K. Singh, A. Soni, J. He, U. V. Waghmare and K. Biswas, *Science*, 2021, **371**, 722–727.
36 Y. Qin, Y. Xiao and L.-D. Zhao, *APL Mater.*, 2020, **8**, 010901.
37 G. J. Snyder, A. H. Snyder, M. Wood, R. Gurunathan, B. H. Snyder and C. Niu, *Adv. Mater.*, 2020, **32**, 2001537.
38 H. Wang, Y. Pei, A. D. LaLonde and G. J. Snyder, *Proc. Natl. Acad. Sci.*, 2012, **109**, 9705–9709.
39 L. Fu, K. Jin, D. Zhang, C. Zhang, H. Nie, Z. Zhen, P. Xiong, M. Huang, J. He and B. Xu, *J. Mater. Chem. A*, 2023, **11**, 24777–24788.
40 B. Qin, W. He and L.-D. Zhao, *J Materiomics.*, 2020, **6**, 671–676.
41 Y. Xiao, D. Wang, Y. Zhang, C. Chen, S. Zhang, K. Wang, G. Wang, S. J. Pennycook, G. J. Snyder, H. Wu and L.-D. Zhao, *J. Am. Chem. Soc.*, 2020, **142**, 4051–4060.
42 A. Zevalkink, D. M. Smiadak, J. L. Blackburn, A. J. Ferguson, M. L. Chabinyc, O. Delaire, J. Wang, K. Kovnir, J. Martin, L. T. Schelhas, T. D. Sparks, S. D. Kang, M. T. Dylla, G. J. Snyder, B. R. Ortiz and E. S. Toberer, *Applied Physics Reviews*, 2018, **5**(2), 021303.
43 Y. Pei, Z. M. Gibbs, A. Gloskovskii, B. Balke, W. G. Zeier and G. J. Snyder, *Adv. Energy Mater.*, 2014, **4**, 1400486.
44 E. O. Kane, *J. Phys. Chem. Solids*, 1957, **1**, 249–261.
45 R. Krause, M. Neubert, Th. Drost, W. Hörstel, A. Polity, F. M. Kiessling, U. Paitz, V. P. Zlomanov and S. Mäkinen, *Mater. Sci. Forum*, 1992, **105–110**, 333–340.
46 A. Polity, R. Krause-Rehberg, V. Zlomanov, V. Stanov, A. Chatchaturov and S. MäKinen, *J. Cryst. Growth*, 1993, **131**, 271–274.

47 Q. Deng, F. Zhang, P. Nan, Z. Zhang, L. Gan, Z. Chen, B. Ge, H. Dong, H. Mao and R. Ang, *Adv. Funct. Mater.*, 2024, **34**(2), 2310073.
48 Y. Xiao, H. Wu, W. Li, M. Yin, Y. Pei, Y. Zhang, L. Fu, Y. Chen, S. J. Pennycook, L. Huang, J. He and L.-D. Zhao, *J. Am. Chem. Soc.*, 2017, **139**, 18732–18738.
49 Y. Qin, T. Hong, B. Qin, D. Wang, W. He, X. Gao, Y. Xiao and L.-D. Zhao, *Adv. Funct. Mater.*, 2021, **31**, 2102185.
50 Z. Zhang, K. Zhao, H. Chen, Q. Ren, Z. Yue, T.-R. Wei, P. Qiu, L. Chen and X. Shi, *Acta Mater.*, 2022, **224**, 117512.
51 C. Zhao, Q. Deng, W. Yuan, X. An, W. Su, Z. He, L. Gan, Y. Xie, Z. Zhao and R. Ang, *J. Mater. Chem. A*, 2024, **12**(15), 9066–9074.
52 D. Zhang, F. Xu, L. Yang, S. Gao, X. San, J.-L. Wang, J. Yang, Y. Luo and S. Wang, *Chem. Mater.*, 2022, **34**(4), 1862–1874.
53 B. Ge, H. Lee, L. Huang, C. Zhou, Z. Wei, B. Cai, S.-P. Cho, J.-F. Li, G. Qiao, X. Qin, Z. Shi and I. Chung, *Advanced Science*, 2022, **9**, 2203782.
54 G. Kresse and J. Furthmüller, *Phys. Rev. B: Condens. Matter Mater. Phys.*, 1996, **54**, 11169–11186.
55 G. Kresse and J. Hafner, *J. Phys.: Condens. Matter*, 1994, **6**, 8245.
56 J. P. Perdew, K. Burke and M. Ernzerhof, *Phys. Rev. Lett.*, 1996, **77**, 3865–3868.
57 P. Hirel, *Comput. Phys. Commun.*, 2015, **197**, 212–219.
58 A. van de Walle, *Calphad*, 2009, **33**, 266–278.